Department of Chemistry
University College London
University of London

Investigation of the Diffusion of Copper into a Gold Nanocrystal by Coherent Diffraction Imaging

Ana Katrina C. Estandarte

Transfer Report
January 24, 2014

Introduction

Nanomaterials are widely used in various applications due to their special properties, which differ from that of the bulk material. Their properties are dependent on their size, composition, and structure. Understanding how the diffusion process works for nanomaterials is of great importance for their stability and controlled synthesis. Diffusion studies by direct conventional methods only give rise to macroscopic information. Although some indirect methods for diffusion studies can give microscopic information, such methods are limited to fast diffusivities and narrow number of isotopes that can be used. Moreover, existing methods for diffusion studies average the signals of a number of structures. However, for nanomaterials, investigating the local structure is important. Hence, there is a need for new techniques that will probe the diffusion process for an individual nanoparticle at the atomic scale.

X-rays have been widely utilised in imaging and structure determination of various materials ranging from biomolecules to materials used in electronics due to its penetrating power and short wavelength that allows the structure of matter to be probed up to atomic resolution. With the emergence of synchrotron radiation sources and free electron lasers, progress in X-ray science is rapidly increasing and new imaging techniques, which were not possible before, are being realized due to the high brilliance of these sources.

One of these techniques is coherent diffraction imaging (CDI). CDI utilises a coherent X-ray beam and due to this coherence, the structure of an individual nanoparticle can be probed without having to use optical elements. From the diffraction pattern measured, the three-dimensional structure of the object can be reconstructed using iterative phase retrieval algorithms.

An important advantage of CDI is its sensitivity to strain within a material. In this study, this strain sensitivity is utilised to investigate the diffusion of copper into an individual gold nanocrystal. The structure of the gold is monitored at different time intervals during the diffusion process. The diffusion of copper is expected to induce lattice distortions in the gold, which is then measurable by CDI thus giving insight into the diffusion process.

2.1 Atomic Diffusion in Nanomaterials

Nanomaterials are defined as those with crystal grain sizes in the range of 100 nm or less. They are of great interest and are widely used in various fields such as biomedicine, catalysis, engineering, and electronics [1-3]. This is due to their unique optical, electronic, magnetic, and chemical properties, which differ significantly from that of their bulk counterparts. These properties such as higher reactivity, higher saturation magnetization, and modified electronic band structures arise from the fact that they have large surface-to-volume ratio.

Understanding how the diffusion process works at the atomic scale for nanomaterials is important in the synthesis and determination of the suitability of the material for specific applications. The properties of nanomaterials depend on their size, structure, composition, and atomic ordering. Thus, investigating the diffusion mechanisms will help in the controlled synthesis of these materials to obtain the desired properties.

There are several conventional methods used to study diffusion in solids (table 1).

Table 1. Experimental methods for direct and indirect diffusion studies in solids [4].

Direct Methods	Indirect Methods
Tracer diffusion plus depth profiling	**Mechanical spectroscopy** (after effect, internal friction, Gorski effect)
Chemical diffusion plus profiling Profiling techniques: - Mechanical and sputter profiling - Secondary ion mass spectrometry (SIMS) - Electron microprobe analysis (EMPA) - Auger electron spectroscopy (AES)	**Magnetic relaxation** (for ferromagnetic materials) **Nuclear magnetic relaxation** (NMR): - Line-shape spectroscopy - Spin lattice relaxation spectroscopy - Spin alignment experiments (SAE)
Spreading resistance profiling (SRP) for semiconductors	**Impedance spectroscopy** (IS) for ion conductors
Rutherford backscattering (RBS)	**Mössbauer spectroscopy** (MBS)
Nuclear reaction analysis (NRA)	**Quasielastic neutron scattering** (QENS)
Field gradient NMR (FG-NMR)	
Pulsed fieldgradient NMR (PFG-NMR)	

Direct methods are based on Fick's laws and investigate diffusion by measuring the profile of the diffusing element in a solid material. They are sensitive to long-range diffusion and only give a macroscopic quantity – the diffusion coefficient.

On the other hand, microscopic information about the diffusion process can be obtained through indirect methods. These methods are not directly based on Fick's law and study phenomena which are influenced by the diffusion jumps of atoms. Quantities such as relaxation times, relaxation rates, and line-widths are measured and from these, the mean residence time of the diffusing atoms is calculated. A microscopic model of the atomic jump process and the diffusivity can then be deduced. Quasielastic neutron scattering (QENS) and Mössbauer spectroscopy (MBS), for example, allows the deduction of the jump direction and jump length of the diffusing atoms as a result of the dependence of the line-width for single crystals on the atomic jump frequency and on the crystal orientation. However, both QENS and MBS are limited to very fast diffusivities (figure 1) and to a narrow number of isotopes. Hence, there is a need for techniques that allow the investigation of the diffusion process at the atomic scale and are sensitive to slower dynamics.

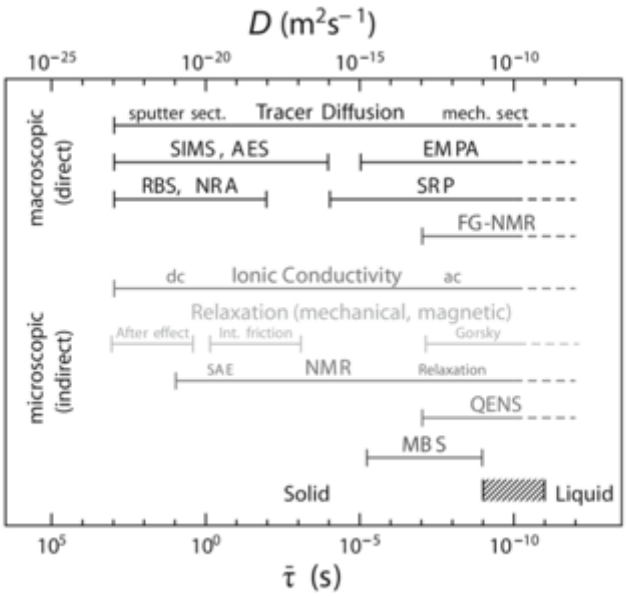

Figure 1. Typical ranges of the diffusivity and mean residence time of direct and indirect methods for diffusion studies [4].

In 2009, the diffusion of single atoms as a function of their neighborhood was studied using X-ray photon correlation spectroscopy (XPCS) [5], which is based on the diffuse scattering of coherent X-rays. This technique does not rely on isotopes and can be applied to most systems. In XPCS, the temporal evolution of fluctuations in the electron density as a function of the wave vector q of the scattered radiation is measured. Since the electron density corresponds to the occupation state of the lattice sites, monitoring the decay times of the electron density as a function of the crystallographic direction will provide information on the diffusive motion of the atoms in the lattice.

2.2 Introduction to X-rays and Synchrotron Radiation

X-rays are widely utilised in various fields, from biological science to materials science, for imaging and structure determination of different materials due to its special properties. It is capable of penetrating through matter and have a much shorter wavelength than visible light thus allowing to resolve structures and produce images with higher spatial resolution. Figure 2 shows that X-rays have the capability of probing structures of matter up to atomic resolution.

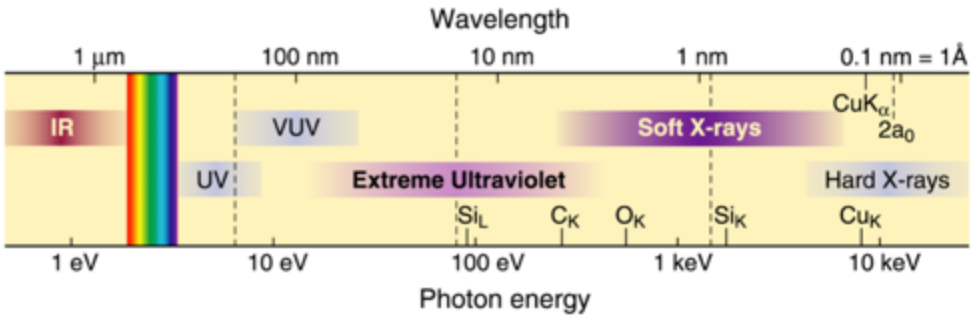

Figure 2. Electromagnetic spectrum showing photon energy and wavelength [6].

The discovery of X-rays by Röntgen in 1895 [7] paved way for a revolution in medical science imaging. He was able to image a bone in the human body. This type of imaging, which is now commonly called X-ray radiography, is based on the absorption of X-rays by matter and the contrast is due to the fact that the absorption is dependent on the atomic number and varies as Z^4. Radiography gives images of local structures in the micro-millimeter length scales. A progress from the conventional radiography was the invention of Computer Axial Tomography (CAT or CT) scanning in the 1970's, which produces three-dimensional images from the two-dimensional radiographic projections of the

object over a wide range of projection angles. Now, CT scanning is widely used for non-invasive diagnosis of injuries and diseases such as diagnosis of breast cancer [8].

Another important interaction of X-rays with matter, which gives rise to other applications of X-rays, is its diffraction by matter. W.H. Bragg and W.L. Bragg observed the diffraction phenomena from a number of crystals in 1913 and laid out the foundations of crystallography [9, 10], which allows crystal structures to be solved from their diffraction patterns. Nowadays, X-ray diffraction is routinely used for structural determination of various materials. For example, a number of protein structures are being solved each year through X-ray diffraction.

Progress in X-ray science increased markedly in the mid 1970's with the realization of synchrotron radiation sources. Synchrotron radiation is a term that describes radiation from charged particles travelling at relativistic speeds in a circular orbit. Inside a storage ring, electrons are stored and kept circulating at certain energy by applied magnetic fields. They travel through straight sections in the ring where they pass through insertion devices (undulators or wigglers) and forced to travel along curved paths in the ring to keep a closed circular orbit by bending magnets leading to the emission of radiation. Radiation is also produced in the insertion devices as the electrons undergo oscillations in these devices due to the alternating magnetic field forces applied to them.

These synchrotron radiation sources have significantly higher brilliance than early lab-based sources (figure 3). Brilliance is a quantity used to characterize the quality of the X-ray beam produced from a source. It combines several aspects, which determine the quality of the X-ray beam: number of photons emitted per second, collimation of the beam (how much the beam diverges), source area, and spectral distribution, and is thus defined as

$$\text{Brilliance} = \frac{\text{Photons/second}}{(\text{beam divergence in mrad})^2(\text{source area in mm}^2)(0.1\%\ \text{energy bandwidth})} \qquad (1).$$

The brilliance from undulator-based third generation synchrotron radiation sources is 10 orders of magnitude higher than that from a rotating anode [11]. Furthermore, synchrotron radiation sources are tuneable thus allowing the optimal wavelength for an

experiment to be selected. The high brilliance and versatility of these sources pave way for the development of new techniques and allow experiments which are not possible before to be carried out. Further progress in X-ray science is expected with the development of free electron lasers which have higher brilliance than the existing sources, higher coherent flux, and pulse lengths of less than 100 fs thus allowing the investigation of time-dependent processes [11].

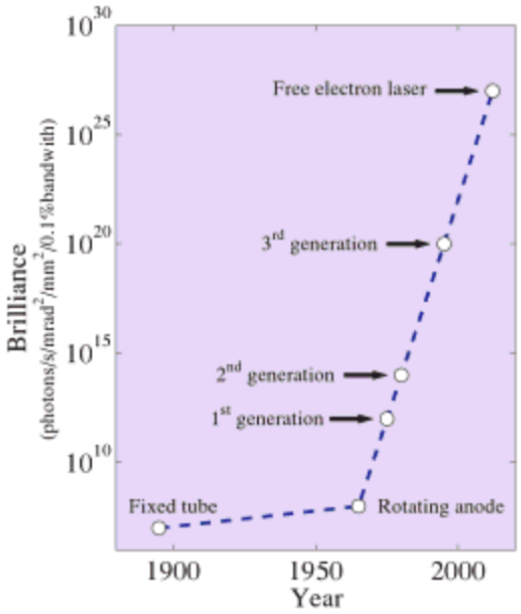

Figure 3. The brilliance of X-ray sources [11].

2.3 Bragg Diffraction from a Crystal and Phase Problem

A crystalline material consists of atoms that form a periodic structure. It can be constructed by regularly repeating a basic structural motif in a three-dimensional lattice. Bragg diffraction in crystals occurs because of the short wavelength of X-rays, which is comparable to the spacing between the lattice planes in the crystal. When a crystalline material is subjected to an incident X-ray beam, the X-ray beam is reflected in a specular manner by the atoms lying at a certain family of lattice planes. In order for diffraction to be observed, the crystal must be oriented in such a way that the Bragg condition is met (figure 4). The Bragg condition states that the path length difference between the waves should be an integer multiple of the wavelength of the incident X-ray beam:

$$m\lambda = 2d \sin \theta \quad (2)$$

where m is an integer, λ is the wavelength, d is the lattice spacing, and θ is the incidence angle of the X-ray beam [9]. Bragg's law is equivalent to Laue's condition (figure 4) which states that diffraction from a crystal can be observed if the scattering vector Q coincides with a reciprocal lattice vector G [11]:

$$Q = G \quad (3).$$

The scattering vector Q is defined as

$$Q = k - k' = 2|k| \sin\theta, \text{ since } |k| = |k'| \text{ for elastic scattering} \quad (4)$$

where k and k' is the incident and scattered wavevector, respectively, while the reciprocal lattice vector G is defined as

$$G = h\,a_1^* + k\,a_2^* + l\,a_3^* \quad (5)$$

where h, k, and l are integers, and a_1*, a_2*, and a_3* are the reciprocal lattice basis vectors.

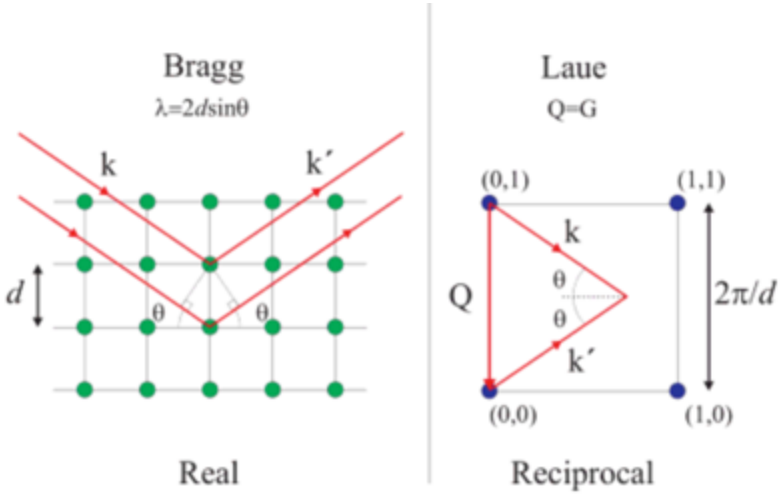

Figure 4. Bragg and Laue conditions for diffraction in crystals [11].

If such conditions are met, constructive interference between the diffracted X-ray beam from individual lattice planes occur and thus, an intense diffracted beam can be observed.

From the diffraction pattern obtained, one can determine the structure of the crystal since the amplitude of the scattered X-ray beam is basically the Fourier transform of the crystal structure. The scattering amplitude for a crystal is defined as

$$F^{crsytal}(Q) = \sum_{l}^{All\ atoms} f_l(Q)\, e^{iQ\cdot r_l} \quad (6)$$

where $f_l(Q)$ is the atomic form factor of the atom at position r_l. The atomic form factor is just the Fourier transform of the electron density, $\rho(r)$, of the atom multiplied by a phase factor $e^{iQ\bullet r}$ (equation 7).

$$f^0(Q) = \int \rho(r)\, e^{iQ\cdot r}\, dr \quad (7)$$

The position of any atom in the crystal, r_l, can be written as $R_n + r_j$ where R_n is the lattice vector and r_j is the position of an atom within the unit cell. Thus, the scattering amplitude can be decomposed into

$$F^{crsytal}(Q) = \sum_j f_j(Q) e^{iQ\cdot r_j} \sum_n e^{iQ\cdot R_n} \quad (8)$$

where the first and second summation corresponds to the unit cell structure factor and lattice sum, respectively.

However, in a diffraction experiment, it is the intensity of the diffracted beam that is measured by the detector and not the amplitude. The amplitude can be represented as a complex number with a modulus, $|F^{crystal}(Q)|$, and a phase, ϕ (equation 9).

$$F^{crsytal}(Q) = |F^{crystal}(Q)|\, e^{i\phi} \quad (9)$$

Since the scattered intensity is equal to the modulus squared of the amplitude

$$I(Q) = F^{crystal}(Q)F^{crystal}*(Q) = |F^{crystal}(Q)|^2 \quad (10),$$

the phase information of the crystal structure factor is lost. Thus, the crystal structure cannot be simply solved by doing an inverse Fourier transform on the measured intensity.

2.4 Coherence

It is important to define what coherence of an X-ray source is as recent imaging techniques in X-ray science rely on the use of coherent or partially coherent sources [12]. If two waves are coherent, they are correlated by a constant relative phase and are thus allowed to interfere with each other either constructively or destructively. Therefore, the coherence of the source can be measured by the visibility of the interference between the waves.

The coherence of the beam can be characterized by two types of coherence length: longitudinal or temporal coherence length L_L and transverse or spatial coherence length L_T.

A beam can deviate from the perfect ideal plane wave either because it is not perfectly monochromatic or it does not propagate in a well-defined direction. Consider the first case where two waves propagating in the same direction have slightly different wavelengths (figure 5).

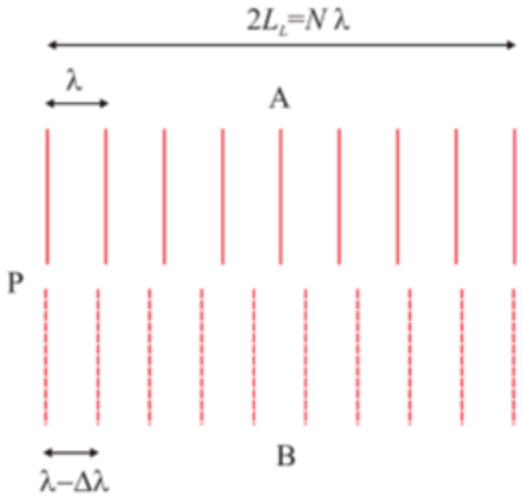

Figure 5. Two plane waves with different wavelengths travelling in the same direction [11].

At point P, these two waves are in phase. After travelling a certain length from point P, the two waves will go out of phase. The distance from point P to the point before the two waves go out of phase is defined as the longitudinal coherence length. After travelling

$2L_L$, the two waves will be in phase again. The longitudinal coherence length can be determined through the equation

$$L_L = \frac{1}{2}\frac{\lambda^2}{\Delta\lambda} \qquad (11).$$

Thus, the longitudinal coherence length depends on the wavelength band of the monochromator.

The other case to consider is where two waves, from a source with a vertical size D and distance R from the observation point P, with the same wavelength propagate in slightly different directions (figure 6).

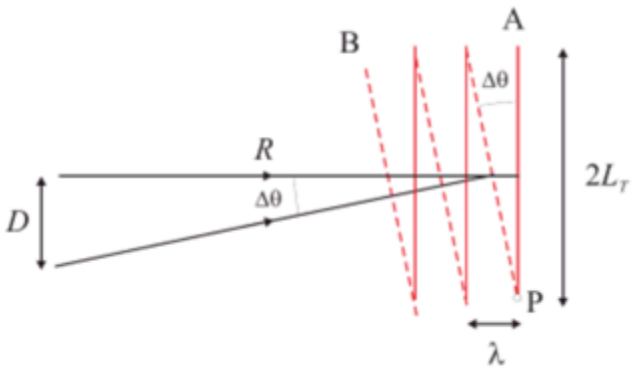

Figure 6. Two waves with the same wavelength propagating in different directions [11].

Again, at point P, these two waves are in phase. The distance from point P, along the wavefront of wave A, to the point before wave A goes out of phase with wave B is called the transverse coherence length. At $2L_T$, the two waves will be in phase again. The transverse coherence length can be calculated through the equation

$$L_T = \frac{\lambda}{2}\frac{R}{D} \qquad (12).$$

Thus, higher transverse coherence length can be achieved by using sources with smaller size and increasing the distance between the source and the sample.

2.5 Coherent Diffraction Imaging

The high brilliance of undulator-based third-generation synchrotron radiation sources, such as the APS and ESRF, and free electron lasers paved way for the realization of modern X-ray imaging techniques, such as coherent diffraction imaging (CDI), which rely on the use of a coherent source. Due to the short wavelength of X-rays, the number of photons present in the coherent volume of the beam, as defined by the transverse and longitudinal coherence lengths, is highly dependent on the brilliance of the source (equation 13).

$$\mathcal{D}_{\text{photon}} = 8.3\text{x}10^{-25}\, \mathcal{B}\, \lambda^3 \qquad (13)$$

where $\mathcal{D}_{\text{photon}}$ is the photon degeneracy and is equal to the number of photons in the coherence volume, and $\mathcal{B}$ is the brilliance of the source. Thus, enough coherent flux can be obtained with these new high brilliance X-ray sources.

CDI is a three-dimensional "lensless" imaging technique which allows the investigation of the local structure of a material, crystalline or noncrystalline. In a conventional diffraction experiment, the information obtained on the structure of the material is an average over a distribution of particles. However, it is important to be able to probe the structure of an individual particle, especially for nanomaterials, as sample heterogeneity can affect the information obtained. High-resolution X-ray microscopy is a technique that can be used to investigate the local structure of materials with a resolution of less than 1 μm. However, such technique requires the use of focussing optics, such as Kirkpatrick and Baez (KB) mirrors [13] and Fresnel zone plates (FZP) [14], which are very hard to fabricate. For example, fabrication of higher resolution FZPs is faced with the technical challenge of minimizing the outermost zone width, which is responsible for the resolution.

Since CDI utilises a coherent source, the local structure of a material can be probed without having to utilise such focussing optics. This is because the incident X-rays are correlated by phase and this correlation is preserved upon the interaction of the X-rays with the sample. The diffracted X-rays from different regions of the sample will have a

fixed relative phase to each other and thus will interfere either destructively or constructively. This interference between the waves is measured by the detector. It is important to note that the sample must be smaller than the coherence volume of the beam for interference effects to be observed. If this is not the case, the total scattered intensity measured will be equal to the sum of the scattered intensities from the different regions of the sample rather than the modulus squared of the sum of the amplitudes. The current spatial resolution that can be achieved with CDI is around 40 nm [12]. Further improvement with the resolution can be expected with the emergence of free electron lasers.

In a Bragg CDI experiment, the crystal and detector are aligned to the desired Bragg peak. A rocking curve of the Bragg diffraction is then obtained by varying the crystal's angle to the beam by a fraction of a degree around its Bragg peak to yield a complete three-dimensional data set. A real space three-dimensional image can then be reconstructed from the diffraction pattern. However, the phase problem in X-ray crystallography applies to CDI as well. As discussed in Section 2.3, it is the intensity of the diffracted beam, which is the squared modulus of the Fourier transform of the structure of the sample, that is measured by the detector thus leading to the loss of phase information needed for the reconstruction of a real space image from the diffraction pattern. In the case of CDI, the phase information can be retrieved, given that the sample is small and finite and the coherence of the beam is sufficient, and the object reconstructed from the Fourier inversion of the diffraction pattern through the use of iterative computer algorithms. These algorithms take the place of the objective lens in a traditional microscope that performs the Fourier inversion to produce an image. Thus, for CDI, there is no need for complex optical elements for the reconstruction of an object.

2.5.1 Oversampling of the Data

In order for the phases to be retrieved using the algorithms, an oversampling requirement must be met. In 1991, Sayre [15] suggested that the phase could be retrieved if the diffraction pattern is oversampled. This was demonstrated experimentally by Miao et al. [16] in 1999 where a reconstruction of a noncrystalline sample, gold dots, was obtained. The oversampling technique was then extended for a crystalline material, gold nanocrystals, by Robinson et al. in 2001 [17]. For phase retrieval to be possible, the

diffraction pattern must be sampled or measured at, at least, twice the Nyquist frequency for one dimension (4x for two dimensions and 8x for three dimensions). Nyquist frequency is defined as the inverse of the system size and is the minimum sampling frequency required for the Fourier transform to invert to the correct object if the magnitude and phase are known. If sampling is done at the Nyquist frequency, the phase problem is underdetermined by a factor of two for one-, two-, and three-dimensional objects, meaning that the set of equations to be solved is half the number of the unknowns.

Sampling at a frequency finer than the Nyquist frequency is only possible if the diffraction pattern is extended in reciprocal space. For a noncrystalline material, the diffraction pattern is a continuous function and thus can be sampled at any Q. However, for a crystalline material, the diffracted intensity can only be observed when Q = G and thus, the intensity on the added sampling points between the Bragg peaks is too weak. If a finite crystal is small enough, oversampling becomes possible as a continuous diffraction pattern is generated and the intensity between the Bragg peaks can be measured.

Miao et al. showed that an oversampled diffraction pattern will inverse Fourier transform to a real space image where a region of no-density around the electron density of the sample is generated [18]. This region of no-density is used to define a real space constraint during the reconstruction process, which will be discussed in the next paragraphs, to retrieve the phase information. As the degree of oversampling is increased, the region of no-density becomes bigger. The oversampling ratio σ, which characterizes the degree of oversampling, is then defined as

$$\sigma = \frac{\text{electron density region} + \text{no-density region}}{\text{electron density region}} \qquad (14).$$

This ratio must be bigger than two for phase retrieval to be possible. In diffraction space, the oversampling ratio can be expressed as

$$\sigma = \frac{\text{fringe size}}{\text{pixel size of the detector}} \qquad (15).$$

Since the fringe spacing is equivalent to λD/S, where λ is the wavelength of the source, D is the distance between the sample and the detector, and S is the size of the sample, equation 15 can be expressed as

$$\sigma = \frac{\lambda D}{(\text{pixel size of the detector})(S)} \qquad (16).$$

Hence, experimentally, the oversampling requirement is met by positioning the detector far enough away from the sample and ensuring that there are at least two detector pixels per fringe.

2.5.2 Phasing Algorithms

As mentioned above, iterative algorithms are used to reconstruct an object from its diffraction pattern. These algorithms are called Hybrid Input-Output (HIO) and Error Reduction (ER), and defined by Fienup in 1982 [19]. They are based on Gerchberg and Saxton algorithm, which was originally developed to retrieve phase information from two intensity measurements (one in real space and one in reciprocal space) [20]. During the reconstruction process, there is an iterative switching between real and reciprocal space through the use of Fast Fourier Transform (FFT) until convergence is reached. Figure 7 shows a diagram of a how the general iterative algorithm works.

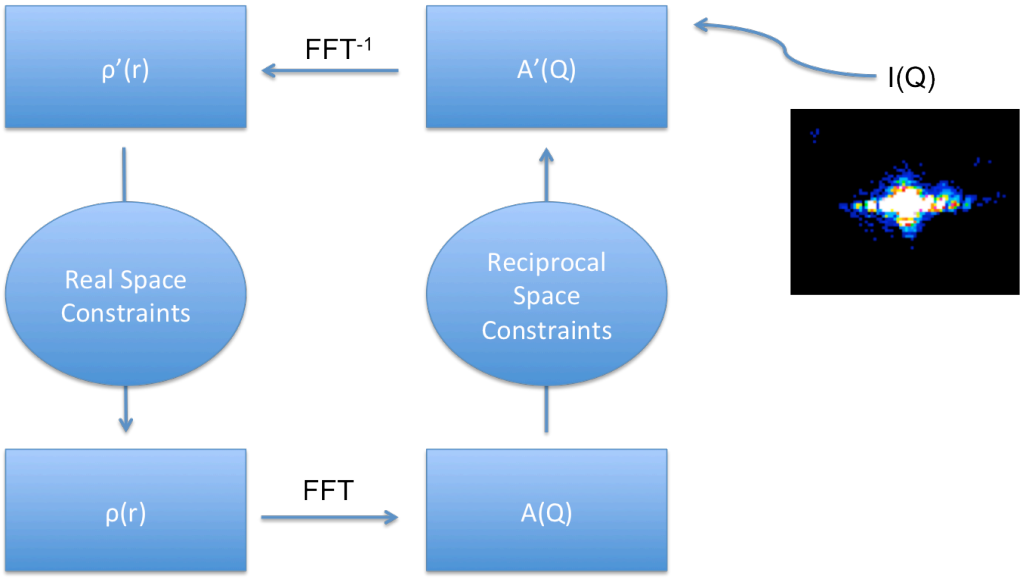

Figure 7. Diagram of how an object is reconstructed from its diffraction pattern.

First, the square root of the measured intensity is multiplied with a random phase factor to obtain an estimate of the scattering amplitude. An inverse FFT is applied to this amplitude to obtain an initial guess of the electron density of the object. Real space constraints are then applied to this electron density. This involves the use of a loose support, which defines the boundary between the no-density region and the electron density of the object described above. The dimensions of the support are estimated directly from the number of pixels in the fringes of the measured diffraction pattern or using autocorrelation methods. A technique called Shrinkwrap [21] allows the support size to be automatically determined as the algorithm progresses. During the iterations, the algorithm gradually drives the electron density outside the support close to zero. Furthermore, a positivity constraint is applied wherein the negative part of the electron density inside the support is also driven close to zero. This is needed in order for a non-trivial unique phase set to be retrieved, as one cannot distinguish a phase and its conjugate from the diffraction intensity alone. After the real space constraints are applied, FFT is applied to the new electron density thus leading to an updated complex scattering amplitude. The phase from this complex amplitude is retained while the modulus is replaced with the square root of the measured intensity. The new complex amplitude is then again propagated to real space and the iterative procedure continues until convergence is achieved. The convergence is measured by an error function.

The ER algorithm decreases the error rapidly for the first few iterations but gets stagnated at some point where the error decreases very slowly. This stagnation problem is prevented by using the HIO algorithm. However, after some iteration in HIO, the improvement in the image quality of the object does not correspond with the reduction in error. Even though the image seems to improve, the error does not decrease. If the HIO iterations are followed by ER iterations, the image quality changes very little but the error will decrease rapidly until it becomes more consistent with the image quality. Hence, in the reconstruction process, one usually uses both HIO and ER algorithms. Recent developments in the algorithms include guided-HIO [22], which improves the reliability of the image of the object, and the ability to correct for partial coherence of the X-ray beam [23].

One of the problems of the HIO algorithm is that the results tend to get trapped in local minima due to noise or when the support used is not tight enough. HIO doesn’t have a

particular way of enforcing the zero-density region inside the loose support to be zero. Hence, different trials of reconstructions could produce different solutions and it becomes very difficult to tell which of these solutions provides the "correct" reconstructed image. A criterion that can be used to determine the accuracy of the reconstructed image is a cost function showing the difference between the calculated intensities and the experimental ones.

A guiding algorithm was developed by Lee and co-workers [24-26] to search for the optimal solution of complex systems. This guiding algorithm involves the use of the cost function to guide the searching pathways for finding the optimal solution. The optimal solution has physical properties that are quite different from most other solutions and these properties can be used to guide the searching path.

By applying an optimization method to the traditional HIO algorithm, one can improve the chances of finding the global minimum [22]. The concept of guided-HIO is to perform many trials of the HIO algorithm using different initial phases and select the solution with the smallest error function in the Fourier space (equation 17) and use it as a template to guide future iterations. The error function is used to determine the quality of the electron density obtained after a certain number of iterations. For example, after *n* iterations,

$$\sigma_n(r) = \begin{cases} |\rho_n(r)|, & if\ r \epsilon S \\ 0, & otherwise \end{cases} \quad (17)$$

where $\rho_n(r)$ is the electron density after the *n*th iteration and S is the support. The error function is then defined as

$$\text{erf}\, F = \frac{\sum_{k \epsilon D} \big||F(k)| - |H_n(k)|\big|}{\sum_{k \epsilon D} |F(k)|} \quad (18)$$

where k is the scattering vector, D is the dataset, |F(k)| is the Fourier modulus, and $|H_n(k)|$ is the Fourier transform of $\sigma_n(r)$.

To demonstrate more clearly, we start with *x* runs consisting of *n* iterations of the HIO algorithm, where each run starts with different initial phases. After *n*/2 number of iterations, a stronger condition is applied to comply with the requirement that the density is positive inside the loose support and zero outside (equation 19).

$$\rho_n(r) = \begin{cases} \rho'_{n-1}(r), & if\ \ r \epsilon S,\ real\left[\rho'_{n-1}(r)\right] \geq 0 \\ \alpha\rho'_{n-1}(r), & otherwise \end{cases} \qquad (19)$$

where α is linearly changed from 1 to 0 in the remaining *n*/2 iterations.

The *x* reconstructed images from the *x* runs are defined as the zeroth generation. The image with the smallest erf F from these runs is selected as the template. For the next generation, the density of the best image, $\rho^{0,template}$, is merged with the other *x-1* reconstructed images by taking the square root of the product of $\rho^{0,template}$ and the *m*th image $\rho^{0,m}$:

$$\rho^{g+1,m}(r) = \sqrt{\rho^{g,template}(r)\ x\ \rho^{g,m}(r)} \qquad (20)$$

where *m* goes from 1 to *x* and *g* stands for the *g*th generation. Through this equation, the density generated in the zero-density region becomes smaller. The new generated images are then used for the next generation and the HIO algorithm is started again. The above procedures are repeated to generate reconstructed images for higher generations.

2.5.3 Strain Sensitivity of CDI

Another advantage of CDI is its sensitivity to distortions in the crystalline lattice thus giving it the ability to image strain in the material in three-dimensions [27-29]. Strain is the spatial derivative of the displacement of the material from an ideal lattice and is caused by chemical, electrical, magnetic, mechanical, and other forces associated with the local environment of the material. The ability to image strain is very important for materials science as a lot of interesting properties of materials result from the strain in the material. The strain sensitivity of CDI was first demonstrated by Pfeifer et al. in 2006 [30] where the deformation field in a Pb nanocrystal was imaged.

If a region in a crystal is strained, the atoms displaced from the ideal lattice will diffract X-rays with a phase shifted from that of the unstrained regions. The phase shift, $\varphi(r)$, is equivalent to $Q \bullet u$, where u is the displacement vector. This phase shift is recorded in the diffraction pattern produced in the vicinity of the Bragg peak due to the coherence of the beam. The diffraction pattern about the Bragg peak will be non-symmetric. The inverse Fourier transform of this non-symmetric pattern generates a complex electron density with a magnitude corresponding to the physical average electron density and a phase corresponding to the local deformations in the crystal lattice along the Q vector of the Bragg peak where the diffraction pattern is measured. Hence, the strained region in the crystal will be manifested in the final image as a region of complex density with the same magnitude from the rest of the crystal but with a phase shift of $\varphi(r)$.

However, CDI is only sensitive to displacements a small fraction of a unit cell in magnitude. Hence, for highly strained crystals with full unit cell displacements, phase wrapping occurs and this has to be unwrapped in order for the displacements to be resolved.

Methodology

3.1 Preparation of Gold Nanocrystals on a Silicon Substrate

Gold nanocrystals were prepared through the dewetting method [17, 29] to obtain an array of isolated nanocrystals on a silicon-wafer substrate. Silicon wafers were first cleaned with a Pirahna solution (a mixture of 3:1 concentrated H_2SO_4 to 30% H_2O_2). 5 nm layer of titanium was then deposited onto the silicon wafer followed by the deposition of 18 nm gold layer through thermal evaporation. The thin film was then annealed in air at 980°C for 12 hours in a laboratory furnace and dewetted from the substrate to form gold nanocrystals with typical size in the range of 100-500 nm, separated by 1 μm.

3.2 CDI Experimental Set-up

The CDI experiments were carried out in the experimental hutch 2 of the I-07 beam line at the Diamond Light Source, UK (figure 8). The sample was placed inside an ultra high vacuum chamber (P = $5x10^{-9}$ mbar), used for in-situ preparations and characterisations, with beryllium windows that are transparent to x-rays. It was mounted on a hexapod sample stage of a 2+3 circle diffractometer, on the horizontal ω-axis resulting to a vertical scattering geometry. The incidence angle of the x-ray beam at the sample was set to 4°. The energy of the x-ray beam was at 9 keV and was selected using a Si-(111) double crystal monochromator with an energy resolution (ΔE/E) of $1.4x10^{-4}$, thus ensuring temporal coherence. For the spatial coherence, a partially coherent beam was defined using a pair of JJ slits, with a size of 15 μm in both the horizontal and vertical directions, placed before the sample chamber. The part of the beam incident on an individual nanocrystal has sufficient coherence even though the incident beam on the sample is only partially coherent because of the very small size of the gold nanocrystals. Deposition of copper onto the gold nanocrystals was achieved using a graphite Knudsen-cell thermal evaporator. Two pieces of 1 cm copper wire were placed inside the evaporator and was heated to 700°C at a pressure of $3x10^{-6}$ mbar. The diffraction pattern from the sample was measured using a Pilatus 100K detector from Dectris, with 487x195 pixels and 172x172 μm^2 pixel size, positioned 1.2 m away from the sample to ensure oversampling which is required for phase retrieval during the reconstruction process. A flight tube, which is under vacuum, is placed between the sample and the detector to reduce the absorption of x-rays by gas molecules that would decrease the number of photons reaching the detector.

a)

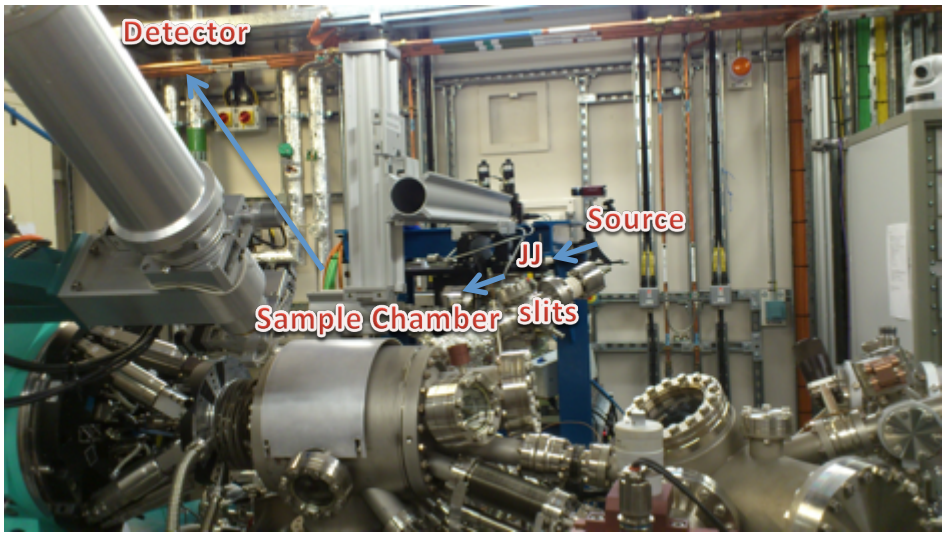
Detector
Source
JJ
Sample Chamber
slits

b)

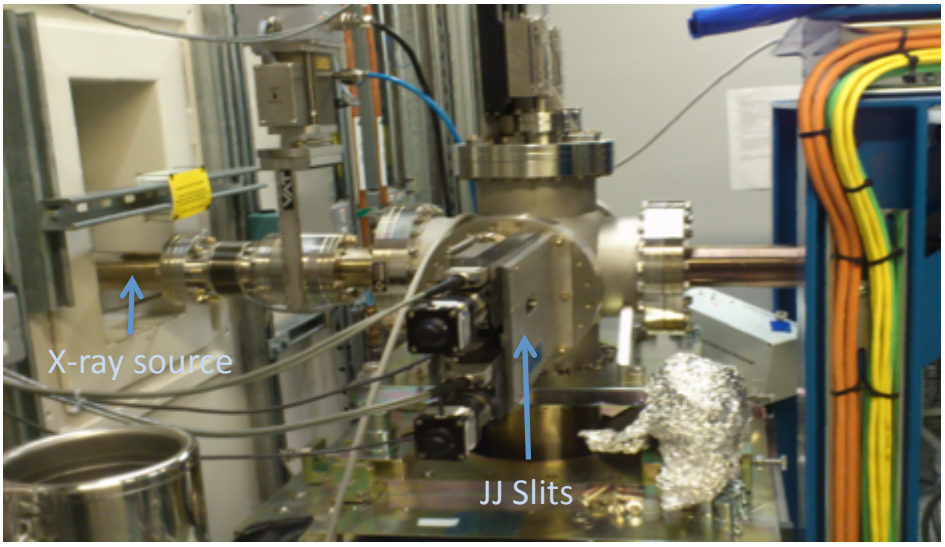
X-ray source
JJ Slits

c) 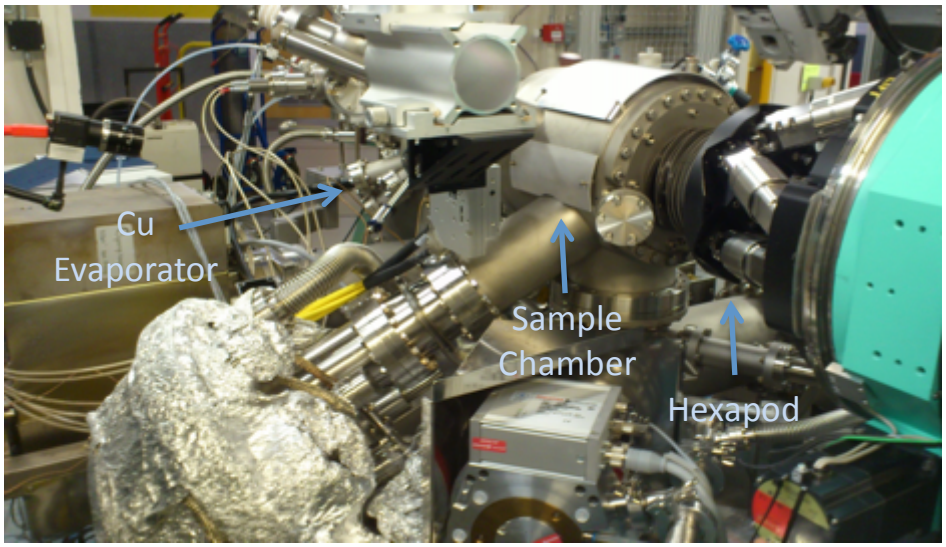

Figure 8. Experimental set-up at the I-07 beamline: a) overview of the path of x-rays from the source to the detector, b) close-up of the source and the JJ-slits, and c) close-up of the sample chamber, hexapod, and Cu evaporator.

3.3 CDI Measurements

The JJ slits and the sample were first aligned. The gold nanocrystals were then measured before the deposition of copper. The sample and the detector were oriented along the gold (111) Bragg reflection. An isolated diffraction pattern was selected. The small beam size and the 4° incidence angle reduced the number of overlapping diffraction patterns caused by crystals that are too close to each other. A rocking curve of the Bragg diffraction was then obtained by an ω-scan, rotating the sample around the Bragg peak in 81 steps of 0.005°, to yield a 3D data set. Copper was then deposited onto the gold nanocrystals for an hour at a sample temperature of 185°C. After which, the sample was measured continuously at the (111) Bragg reflection at 300°C and 340°C for several hours to observe the diffusion process as a function of time for each temperature.

3.4 Reconstruction of the Gold Nanocrystals

The measured diffraction patterns from a rocking curve series were stacked in one image using ImageJ. The diffraction pattern from the nanocrystal of interest was cropped resulting to a 72 x 64 array size. A total of 80 frames were used, which defines the array size in the z-dimension. The phasing algorithms were performed on this array size using MATLAB. No binning was done on the data. A flat support with the dimensions of 32.4 x 22.4 x 36 pixels was used as a real space constraint and this support was allowed to

evolve during the iterations using Shrinkwrap. Shrinkwrap was applied every five iterations and the iterations in between were fixed. A guided approach was used together with the ER and HIO algorithms. Eight independent runs consisting of 200 iterations each were performed. Each run has a different starting phase. The 200 iterations started with ER. The algorithm was switched to HIO at the 5^{th} iteration and was switched back to ER at the 180^{th} iteration. The best reconstructed image from the eight runs was used as a template for the next generation of eight independent runs. A total of five generations were done. The resulting phased 2D slices were aligned and reconstructed into a 3D image using Mayavi.

Isolated gold nanocrystals with a size range of 100-500 nm were prepared using the dewetting method (figure 9). The SEM image shows that the nanocrystals obtained have spherical or curved regions and flat facets.

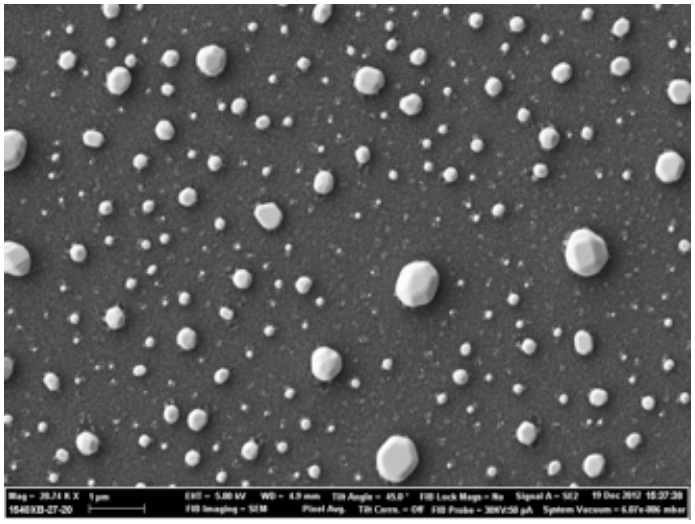

Figure 9. SEM image of the gold nanocrystals.

Figure 10 shows the diffraction pattern obtained from an individual gold nanocrystal at the center of the rocking curve measured around the (111) Bragg reflection of the nanocrystal.

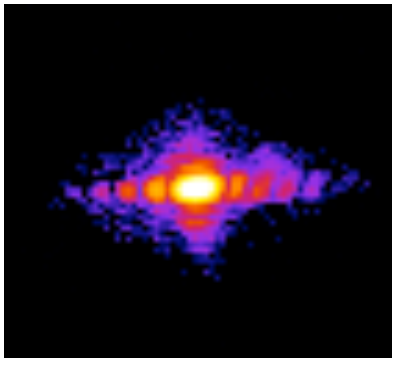

Figure 10. Center of the rocking curve measured around the (111) Bragg reflection of an individual gold nanocrystal.

It can be observed that the obtained diffraction pattern is fairly symmetric about its center. This symmetry arises from the inversion symmetry of the magnitude of the

Fourier transform of a real object and is lost upon moving away from the center of the rocking curve [31]. Moreover, the diffraction pattern is characterized by fringes of modulation and radial flares of intensity. The radial pattern results from the sphericity of the crystal while the fringes arise from the coherence of the beam incident to the sample, which allows the interference of scattered waves from all parts of the sample. Since the crystal dimensions are small, it was ensured that the beam incident to the nanocrystal was fully coherent. If the beam is not fully coherent, the visibility of these modulations is reduced. The strong flare in the diffraction pattern results from the enhancement of intensity along the direction of the nanocrystal facets. It points in the crystal's (111) direction, which is normal to the substrate surface. The characteristic features observed from the diffraction pattern signify that the nanocrystal measured is fairly unstrained. It will be shown later on that the presence of strain results to the loss of these features.

From the measured diffraction pattern, the gold nanocrystal was reconstructed using the phasing algorithms error reduction and hybrid input-output with and without the use of a guided approach. The recovery of the phase from the measured intensity data was possible by oversampling the diffraction pattern. A gold nanocrystal with a size of 500 nm, which is the largest possible size of the synthesized nanocrystals, gives an oversampling ratio of 1.92 using equation 16 for the parameters used in the experiment (sample to detector distance = 1.2 m and wavelength = 1.38 Å), which is just enough for phase recovery. Smaller gold nanocrystals would give higher oversampling ratios (eg. for a 100 nm nanocrystal, $\sigma = 9.6$). The fringes in the measured diffraction pattern in figure 10 contain 2, 4, and 3 pixels per fringe in x-, y-, and z-dimensions, respectively. Furthermore, a finite support with a dimension of 32.4 x 22.4 x 36 pixels was used as a real-space constraint during the reconstruction process giving an oversampling ratio of 2.22, 2.86, and 2.22 in the x-, y-, and z-dimensions, respectively.

The difference between the guided and unguided approach is that five generations of eight independent runs of 200 iterations consisting of HIO and ER were done for the guided algorithm while only one run of 200 iterations of HIO and ER was done for the unguided algorithm. Figure 11a, 11b, and 11c show the reconstructed amplitudes from three independent runs of the unguided algorithm. The solutions obtained are quite different from each other, although a common feature is present. This is due to the tendency of the solution being the local minimum instead of the global minimum when

the HIO algorithm is used. Furthermore, it can also be seen that there is a density fluctuation inside the nanocrystal using the unguided algorithm. The 3D reconstruction of the gold nanocrystal at 0.25-threshold level from one of these runs is shown in figure 12. Figure 12 shows that the nanocrystal did not reconstruct completely as there are missing parts. The error after the 200th iteration for the three unguided runs is around 2.1x10^{-2}. Figure 11d shows the reconstructed amplitude from a run of the guided algorithm. The solution obtained is almost the same after five trials. It is observed from the image that the amplitude is almost uniform across the nanocrystal. The error obtained from the guided algorithm is 1.8x10^{-3}. This error can be further reduced by increasing the number of generations and the number of independent runs of ER and HIO per generation.

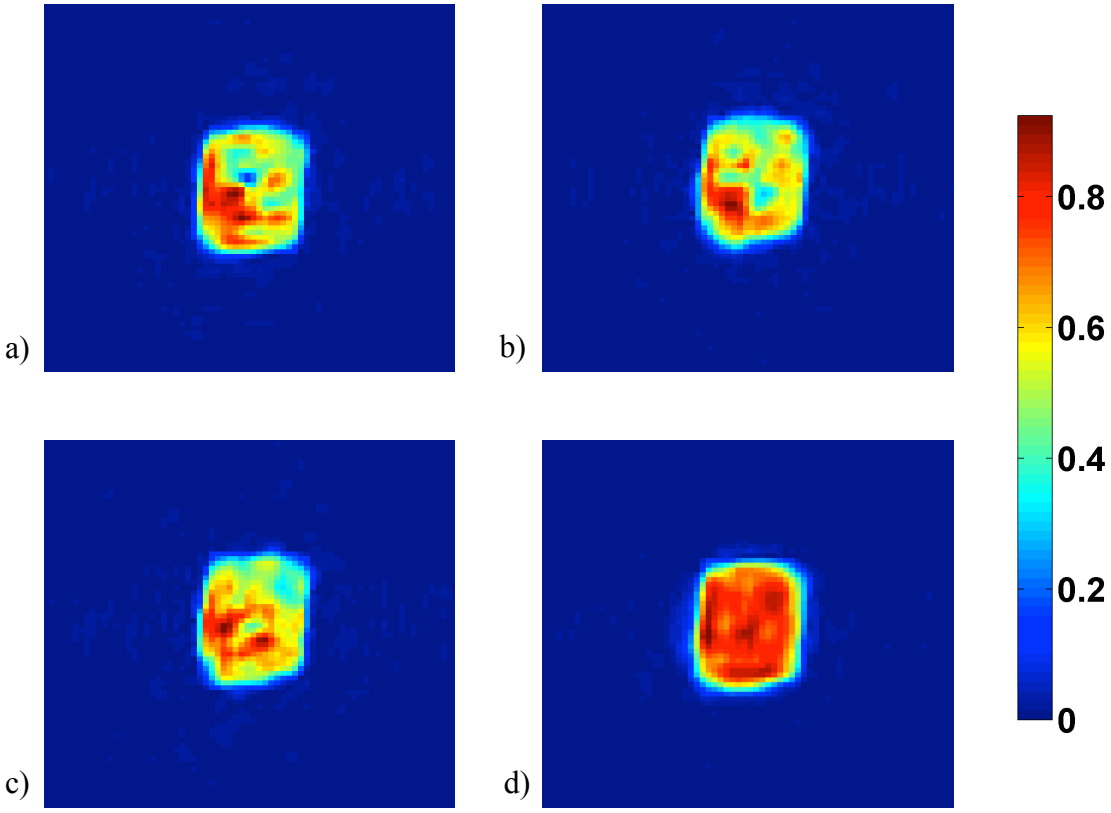

Figure 11. Reconstructed amplitudes near the center of the gold nanocrystal before copper deposition (xz plane) using a-c) ER and HIO, and d) ER and HIO with a guided approach.

a) 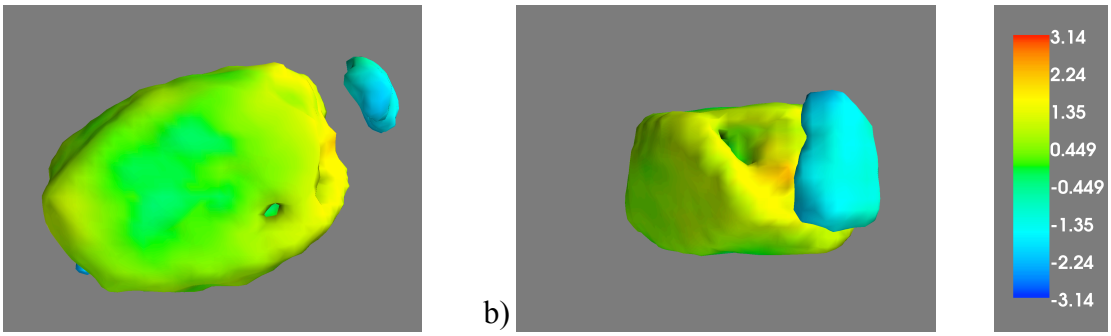

b)

Figure 12. Phase isosurface image of the reconstruction of the gold nanocrystal without the guided approach before copper deposition: a) top view, and b) side view.

Figure 13 shows an isosurface image of the reconstructed gold nanocrystal before copper deposition at 0.25-threshold level using the guided approach. The color represents the phase of the complex amplitude showing the surface variation of the imaged component of the displacement field.

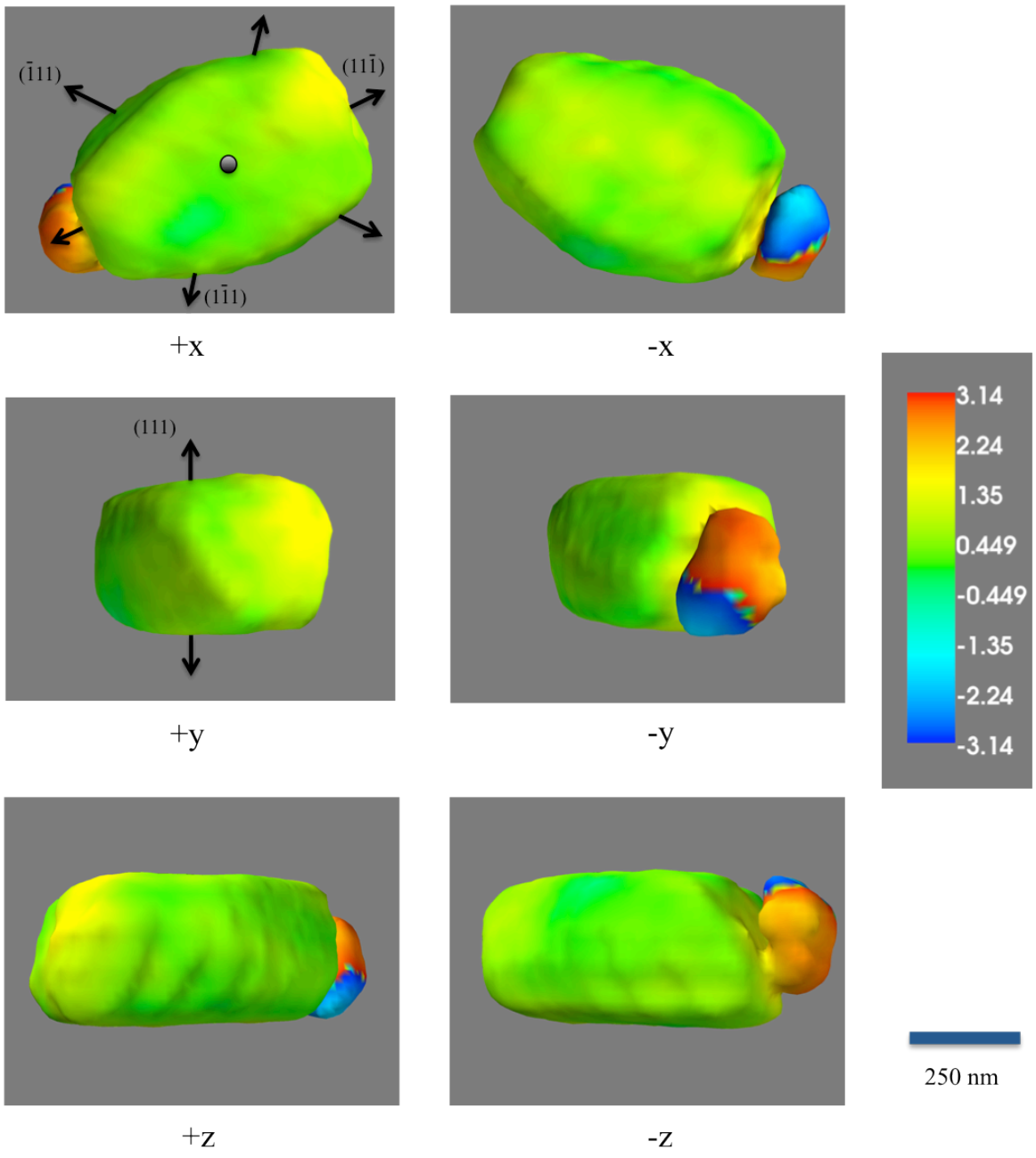

Figure 13. Phase isosurface reconstruction of the gold nanocrystal before copper deposition using the guided approach. The six images show the different views. The {111} directions are represented as arrows in the first image. The arrows in the +y view show the direction of the (111) and ($\bar{1}\bar{1}\bar{1}$) facets. The phase range is from π (red) to -π (blue).

The reconstructed gold nanocrystal has a structure similar to that seen in the SEM image in figure 9. Its morphology is characterized by an elongated oval shape with eight flat facets facing the {111} directions as represented by the arrows in figure 13 (first image),

and curved regions where the facets meet. The nanocrystal has larger (111) and ($\bar{1}\bar{1}\bar{1}$) facets than the other six off specular side facets and measures 267 nm in the x-axis (height), 534 nm in the y-axis (length), and 334 nm in the z-axis (width). The extended (111) and ($\bar{1}\bar{1}\bar{1}$) facets and the curved regions signify that the true equilibrium crystal shape has not been reached [32], possibly due to incomplete dewetting. Furthermore, it can be observed that there is a small piece of object, which has a shape that looks like half of a sphere, separated by a gap from the ($\bar{1}\bar{1}1$) facet. This piece could be a part of the nanocrystal and the gap in between may be due to the different stacking/orientation of the lattice planes, which would cause these planes to "disappear" since the measurements are done in the (111) Bragg peak of the nanocrystal [33]. The gap can also be due to a part of the nanocrystal being sliced off. The different stacking of the planes in the gap or the slicing off of the nanocrystal in this gap would both cause the small piece to be highly strained. This strain is seen from its phase, which appears as a sudden phase jump from the rest of the nanocrystal whose phase appears quite flat. The flat phase of the rest of the nanocrystal signifies that across this region, the nanocrystal is relatively unstrained, which agrees with the symmetric diffraction pattern presented above. The maximum phase within this region is around 1.35 radians, which corresponds to a displacement of 0.05 nm from the ideal lattice along the projection of Q. This is less than a quarter of the (111) lattice spacing of gold (d = 0.24 nm). The higher phase values are observed more at the edges where the curved regions are found and the facets meet, and at the bottom of the nanocrystal (-x view). The strain at the bottom of the nanocrystal can be due to the stress induced by the substrate resulting from lattice mismatch between gold and the substrate.

The same gold nanocrystal presented above was monitored after an hour of copper deposition. Figure 14 shows a plot of the sum of intensity across the region of interest versus the omega angle before copper deposition (control), and 3 hours and 6 hours after the deposition. The plot shows that as diffusion proceeds, the (111) Brag peak of the gold nanocrystal shifts to lower values of omega thus signifying that the lattice parameter of the nanocrystal is increasing. This is due to the lattice displacements induced by the copper atoms within the gold lattice. Furthermore, a decrease in the measured intensity and broadening of the Bragg peak can also be observed, and after 6 hours of diffusion, the peak starts to split in two signifying that the crystal starts to be multi-centered.

These changes in the Bragg peak of the gold nanocrystal signify the loss of crystalline material and presence of strain.

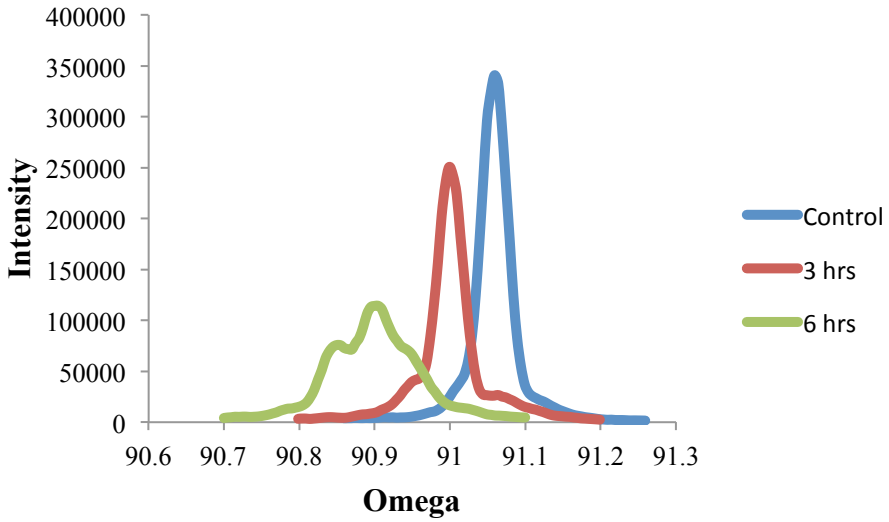

Figure 14. Measured intensities across the rocking curve series of the gold nanocrystal before and after copper deposition.

Figure 15 shows a time series of the measured diffraction patterns at the center of the rocking curve around the (111) Bragg peak of gold after the deposition of copper onto the gold nanocrystal at a sample temperature of 300°C.

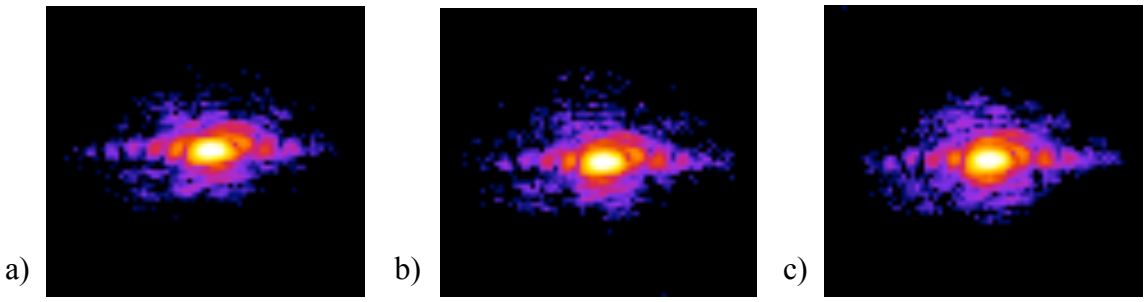

Figure 15. Diffraction patterns obtained from the gold nanocrystal: a) 1 hr, b) 2 hrs, and c) 3 hrs after copper deposition at a sample temperature of 300°C.

Comparing the measured diffraction patterns in figure 15 with the diffraction pattern from the gold nanocystal before copper deposition (figure 10), it can be observed that there are only subtle changes in the diffraction pattern after 3 hours of diffusion at 300°C. The fringes are starting to become less visible. The sample temperature was then raised to

340°C without further copper deposition and the same gold nanocrystal was measured (figure 16).

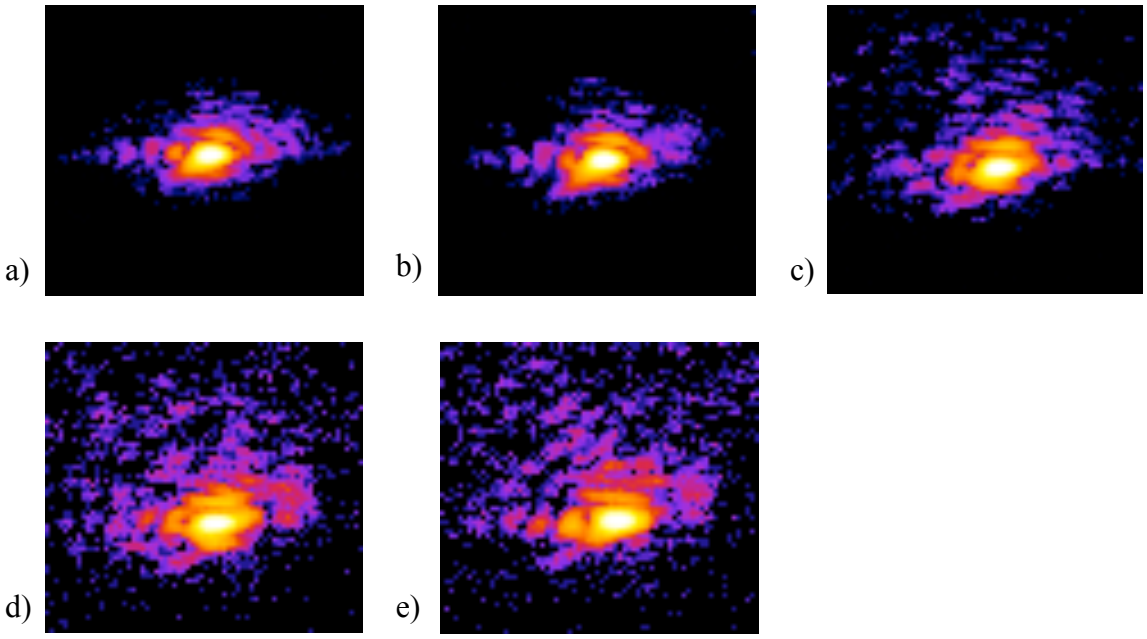

Figure 16. Diffraction patterns obtained from the gold nanocrystal: a) 4 hrs, b) 5 hrs, c) 6 hrs, d) 7 hrs, and d) 8 hrs after the initial copper deposition at a sample temperature of 340°C.

Figure 16 shows that, as the diffusion process proceeds, the diffraction pattern becomes more asymmetrical. This signifies that the copper atoms are diffusing into the gold lattice thus causing lattice distortions within the gold nanocrystal. It was discussed earlier that strain causes an object to be complex valued thus resulting to the loss of the centrosymmetry of its amplitude. The lattice distortions due to the diffusion process also results to the fringes being no longer along the crystal axes as the flat facets gradually disappear. It can also be observed that the center of the diffraction pattern becomes less spherical and after 8 hours of diffusion, the pattern is no long single-centered.

The phase diagram for gold-copper system (figure 17) shows that there are two possible ordered alloys that can be formed at 340°C: CuAu and Cu_3Au. The presence of copper on the gold nanocrystal was confirmed by the presence of a copper powder ring (figure 18a). Furthermore, the formation of the Cu_3Au alloy is suggested due to the presence of a diffuse spot at the (100) Cu_3Au peak (figure 18b). Hence, there is an ordering of the copper atoms within the gold lattice during the diffusion process.

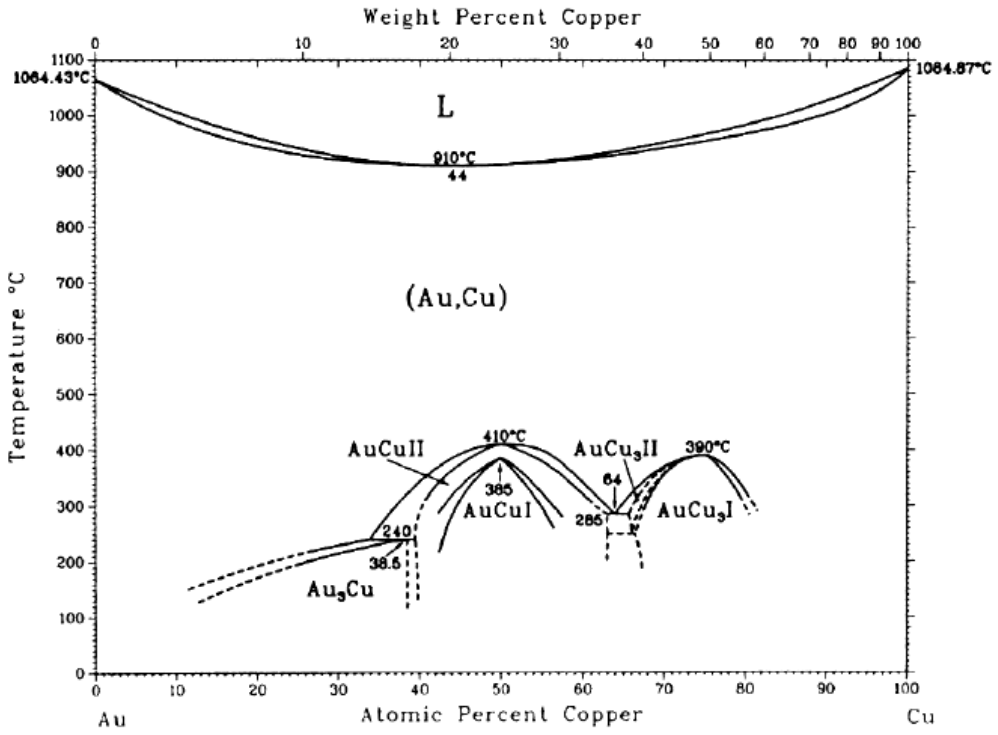

Figure 17. Phase diagram of the gold-copper system [34].

a) 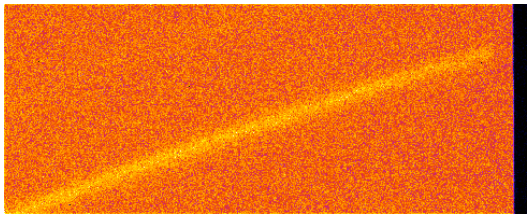 b) 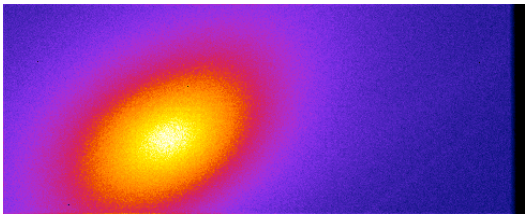

Figure 18. Powder ring of a) copper, and b) Cu_3Au.

Figure 19 shows a time series of scalar cut planes (xz planes) of the reconstructed amplitudes near the center of the gold nanocrystal using the guided approach.

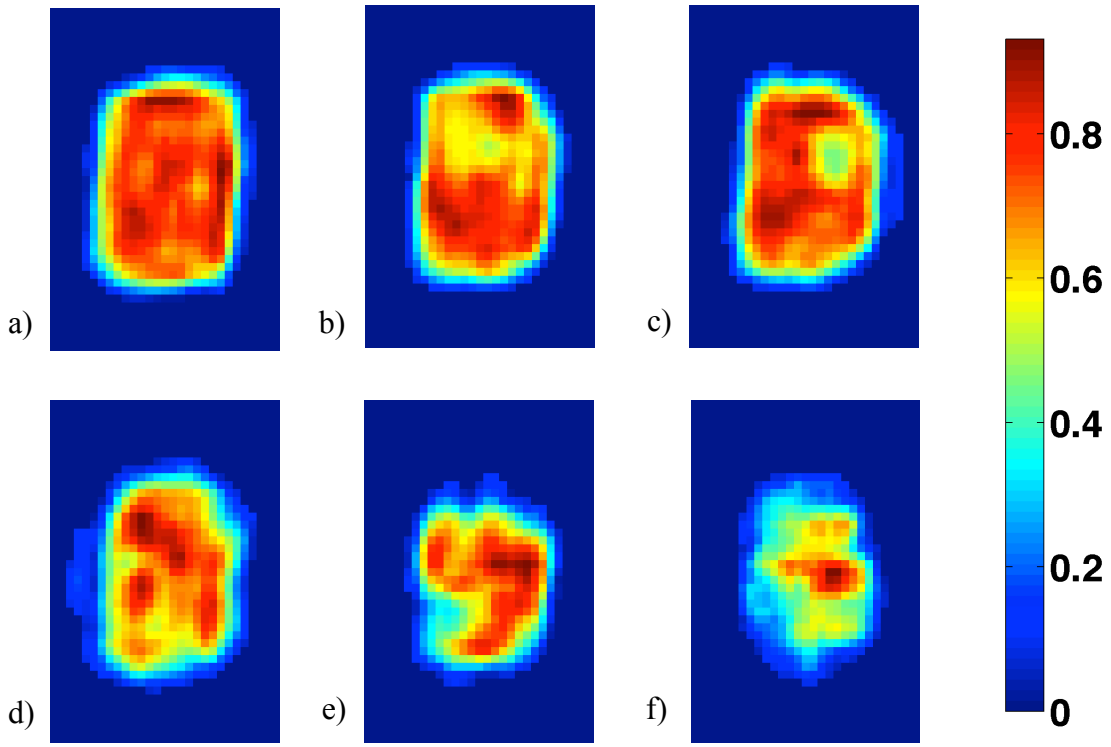

Figure 19. Reconstructed amplitude of the gold nanocrystal a) before copper deposition, and b) 1hr, c) 2hrs, d) 3 hrs, e) 4 hrs, and f) 6 hrs after deposition.

It can be observed that before copper deposition, the amplitude inside the nanocrystal is uniform. As the diffusion process proceeds, the total amplitude inside the nanocrystal decreases as the frequency of the peak value of the amplitude decreases and regions with lower amplitude values begin to appear thus causing the distribution of the amplitude values within the nanocrystal to be broader. This signifies an increase in the variation of density within the nanocrystal.

Furthermore, the nanocrystal appears to shrink in volume. Figure 20 shows the volume of the nanocrystal at a given point in the time series. The volumes are calculated from the reconstructed amplitudes and normalized to the value before the copper deposition. After 7 hours of diffusion, the volume of the nanocrystal decreased to 52% of its volume before copper deposition.

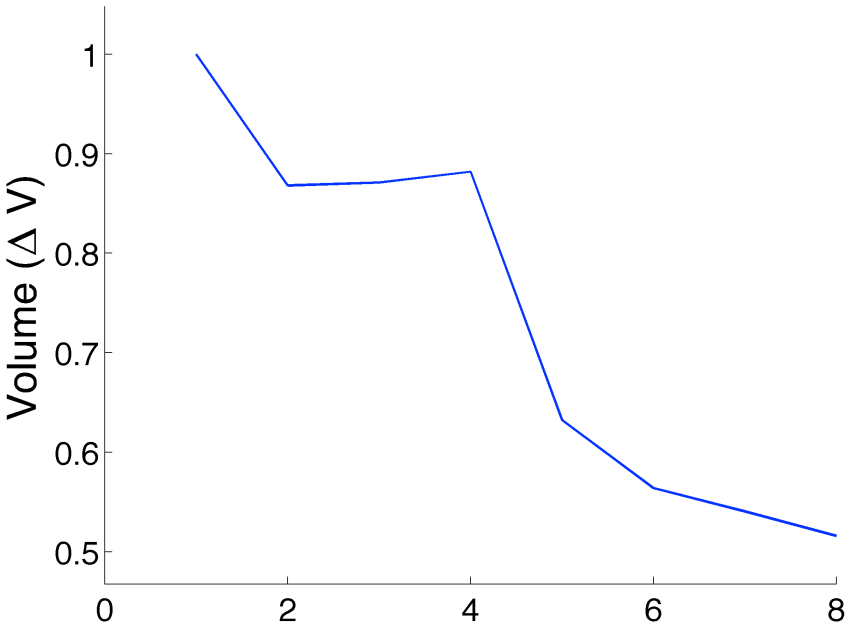

Figure 20. Decrease in the volume of the gold nanocrystal as the diffusion process proceeds. The x-axis represents points in the time series with point 1 as the nanocrystal before copper deposition and points 2 to 8 are the time series after copper deposition. Point 8 represents the nanocrystal after 7 hours of diffusion.

The shrinking of the volume and the broadening of the amplitude distribution within the nanocrystal is due to the fact that the diffraction measurements are done in the (111) Bragg peak of gold, thus only the gold crystalline part will contribute to the signal. The amplitude images hence signify that the alloy formation resulting from the diffusion of copper leads to the removal of the gold crystalline material and formation of new structures with new lattice constants and orientations.

A time series of the reconstructed phase images using the guided approach, also shown as scalar cut planes (xz planes), near the center of the gold nanocrystal are presented in figure 21.

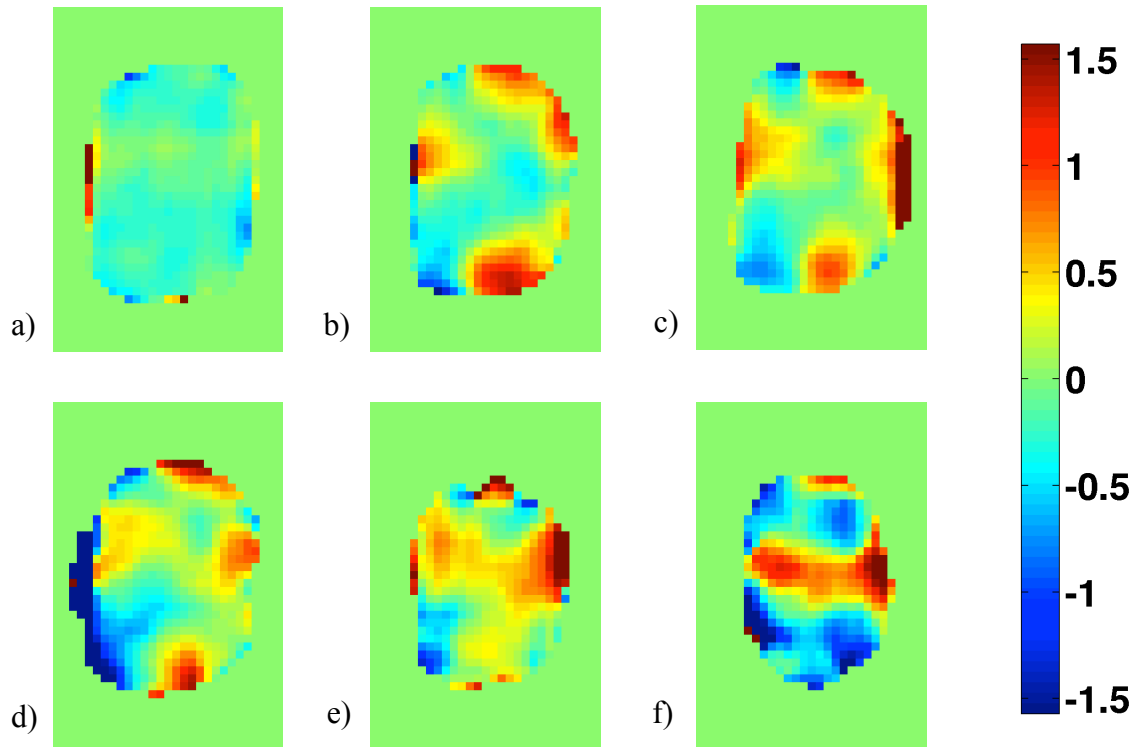

Figure 21. Reconstructed phase of the gold nanocrystal a) before copper deposition, and b) 1hr, c) 2hrs, d) 3 hrs, e) 4 hrs, and f) 6 hrs after deposition. The phase ranges from 1.5 (red) to -1.5 (blue) radians. Positive values represent displacements along the projection of Q while negative values represent displacements in the opposite direction.

Figure 21 shows that before copper deposition, the inside of the gold nanocrystal is relatively unstrained and phases of about ± 0.5 radians are present in the edges where the facets meet. After an hour of diffusion, it can be observed that there are three yellow regions with a phase of 1.5 radians. As the diffusion process proceeds, these regions start to meet. In between these yellow regions, there is phase jump to -1.5 radians. After 6 hours of diffusion, the inside of the crystal is no longer strain free. The appearance of the yellow regions and the phase jump corresponds to the formation of dislocation loops upon the insertion of a single plane of copper atoms over a small region between two adjacent gold lattice planes, and the relaxation of the strain field surrounding it [35, 36]. The formation of the dislocation loops started near the edges where strain is initially present. The diffusion of copper atoms at these regions is easier since the atomic jump process is mediated by defects [4, 37].

Figure 22 shows the top view of the isosurface images of the reconstructed gold nanocrystal using the guided approach before and after copper deposition. The volume shrink of the nanocrystal discussed above can be seen in the 3D reconstructions. The surface of the nanocrystal becomes rougher and the flat facets gradually disappear as diffusion proceeds. The surface of the nanocrystal becomes highly strained after 6 hours of diffusion.

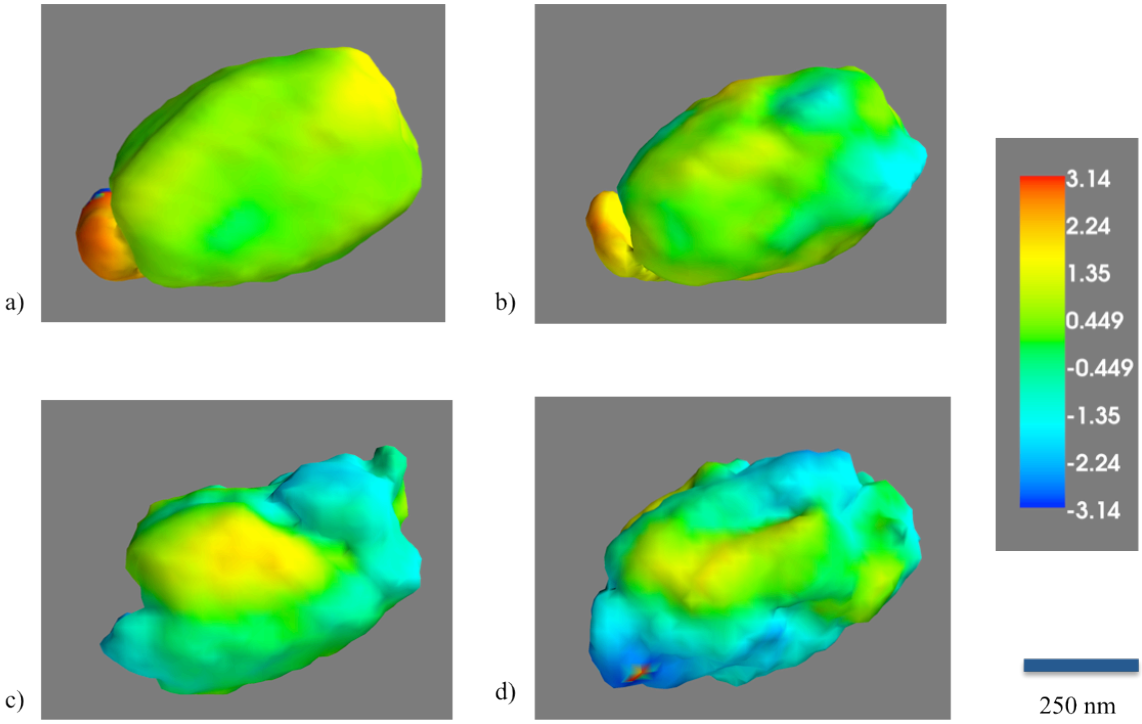

Figure 22. Top view of the phase isosurface images of the reconstructed gold nanocrystal a) before copper deposition, and b) 3 hrs, c) 4 hrs, and d) 6 hrs after deposition.

Future Work

It has been shown in this transfer report that CDI is a technique that can be used to study the structure of an individual nanocrystal and to see changes in this structure through CDI's ability to image strain. Future studies will be directed towards the investigation of the structure of various nanoparticles using CDI.

One of the systems that will be studied in the future is the gold-platinum system. Gold and platinum nanoparticles are known as catalysts for important chemical reactions (e.g. CO and methanol oxidation for gold [38] and oxygen reduction reaction (ORR) for platinum [39]) involved in fuel cell applications. These catalysts, however, have limited catalytic efficiency when used alone: gold having exclusive activity for CO, and platinum being expensive and unstable during the ORR reaction. It has been shown that synergistic catalytic activity can be achieved through alloying of gold and platinum [40, 41]. These two metals are immiscible in the bulk state [34] but the unique thermodynamic properties of nanoparticles allow their alloying in the nanoscale [42] thus leading to a multifunctional catalyst with enhanced stability and catalytic efficiency.

The structure, composition and phase properties of bimetallic nanoparticles are critical in tuning their catalytic properties [43]. However, in spite of the active research on AuPt nanoparticles, there is still a lack of understanding on their structure, composition, and phase properties and how these are affected by various factors. There is still a question on whether phase segregation occurs causing the particles to form core-shell structures especially at high temperatures (figure 23). Hence, it is of great importance to understand how the diffusion process works at the atomic scale for these nanoparticles for their controlled synthesis to obtain the desired catalytic properties.

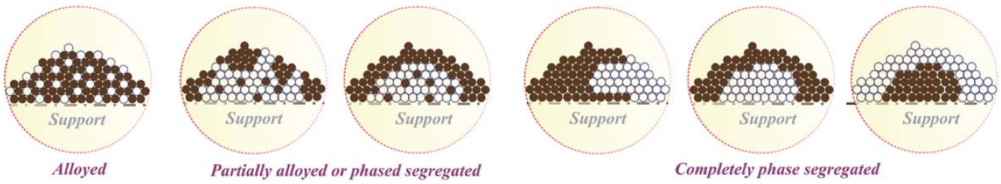

Figure 23. For Au_nPt_{100-n} nanoparticles supported on a certain type of support materials, the nanoscale alloying or phase segregation could lead to the formation of several possible states [42].

CDI will be utilised to investigate the diffusion of platinum into an individual gold nanocrystal. The gold-platinum system will be different from the gold-copper system as gold and copper are miscible and thus are expected to end up as a complete alloy while gold and platinum are immiscible in the bulk state. Hence, it will be interesting to see how the alloying of gold and platinum occur at the nanoscale and any surface alloy detected will be a new result.

Beam time at the I-07 beamline at the Diamond Light Source, UK has already been allocated this year. Gold nanocrystals will be prepared through the dewetting method. The same experimental set-up with that of the gold-copper experiment will be used. Deposition of platinum onto the gold nanocrystals will be achieved using an electron-beam evaporator. The structure of the gold nanocrystal will be monitored as a function of time and temperature during the diffusion process. After which, measurements will be made at the Bragg peaks of the possible alloys to study the structure of the alloys formed.

Force field theory and density functional theory (DFT) simulations will be performed on the gold-platinum system to see which possible structures will be formed upon mixing of gold and platinum and which of these structures will be more thermodynamically favorable. Effect of temperature and composition in the structures will also be investigated. This will lead to a possible collaboration with Richard Catlow's group as one of his PhD students Anna Gould, who is also under the EngD Molecular Modelling and Materials Science program, does this type of simulations. She investigated the chemical ordering of $(AuAg)_{147}$ nanoalloys using DFT and the difference in energies between alloy and core-shell structures was calculated and the most thermodynamically stable structure had been determined.

References

[1] Q.A. Pankhurst, et al., J. Phys. D: Appl. Phys., 36 (2003) R167-R181.

[2] I. Robinson, et al., Chem. Matter., 21 (2009) 3021-3026.

[3] N. Pazos-Perez, et al., J. Mater. Chem., 20 (2010) 61-64.

[4] H. Mehrer, Diffusion in Solids, Springer, Germany, 2007.

[5] M. Leitner, B. Sepiol, L.M. Stadler, B. Pfau, G. Vogl, Nature Materials, 8 (2009) 717-720.

[6] D. Attwood, Soft X-rays and Extreme Ultraviolet Radiation: Principles and Applications, Cambridge University Press2007.

[7] W.K. Röntgen, Science, New Series, 3 (1896) 726-729.

[8] J.M. Kinsella, R.E. Jimenez, P.P. Karmali, A.M. Rush, V.R. Kotamraju, N.C. Gianneschi, E. Ruoslahti, D. Stupack, M.J. Sailor, Angewandte Chemie-International Edition, 50 (2011) 12308-12311.

[9] W.H. Bragg, W.L. Bragg, Proceedings of the Royal Society of London Series a-Containing Papers of a Mathematical and Physical Character, 88 (1913) 428-438.

[10] W.L. Bragg, Proceedings of the Royal Society of London Series a-Containing Papers of a Mathematical and Physical Character, 89 (1913) 248-277.

[11] J.a.M. Als-Nielsen, D., Elements of Modern X-ray Physics, John Wiley & Sons, Ltd, United Kingdom, 2011.

[12] I. Robinson, R. Harder, Nature Materials, 8 (2009) 291-298.

[13] P. Kirkpatrick, A.V. Baez, Journal of the Optical Society of America, 38 (1948) 766-774.

[14] A.V. Baez, Journal of the Optical Society of America, 51 (1961) 405-&.

[15] D. Sayre, NATO ASI Ser. Ser. B (Physics), 274 (1991) 353-356.

[16] J.W. Miao, P. Charalambous, J. Kirz, D. Sayre, Extending the methodology of X-ray crystallography to non-crystalline specimens, in: P. Pianetta, J. Arthur, S. Brennan (Eds.) Synchrotron Radiation Instrumentation2000, pp. 3-6.

[17] G.J. Williams, M.A. Pfeifer, I.A. Vartanyants, I.K. Robinson, Physical Review Letters, 90 (2003).

[18] J. Miao, D. Sayre, Acta Crystallographica Section A, 56 (2000) 596-605.

[19] J.R. Fienup, Applied Optics, 21 (1982) 2758-2769.

[20] R.W.a.S. Gerchberg, W. O., Optik, 35 (1972) 237-246.

[21] S. Marchesini, H. He, H.N. Chapman, S.P. Hau-Riege, A. Noy, M.R. Howells, U. Weierstall, J.C.H. Spence, Physical Review B, 68 (2003).
[22] C.C. Chen, J. Miao, C.W. Wang, T.K. Lee, Physical Review B, 76 (2007).
[23] J.N. Clark, X. Huang, R. Harder, I.K. Robinson, Nature Communications, 3 (2012).
[24] C. Chou, R. Han, T. Lee, S. Li, A guided Monte Carlo approach to optimization problems, Intelligent Data Engineering and Automated Learning, Springer2003, pp. 447-451.
[25] C. Chou, R. Han, S. Li, T.-K. Lee, Physical Review E, 67 (2003) 066704.
[26] C.I. Chou, T.K. Lee, Acta Crystallographica Section A, 58 (2002) 42-46.
[27] W. Cha, N.C. Jeong, S. Song, H.-j. Park, T.C.T. Pham, R. Harder, B. Lim, G. Xiong, D. Ahn, I. McNulty, Nature materials, 12 (2013) 729-734.
[28] I. Robinson, Journal of the Physical Society of Japan, 82 (2013) 1012.
[29] M. Watari, R.A. McKendry, M. Vogtli, G. Aeppli, Y.A. Soh, X.W. Shi, G. Xiong, X.J. Huang, R. Harder, I.K. Robinson, Nature Materials, 10 (2011) 862-866.
[30] M.A. Pfeifer, G.J. Williams, I.A. Vartanyants, R. Harder, I.K. Robinson, Nature, 442 (2006) 63-66.
[31] I.K. Robinson, I.A. Vartanyants, G. Williams, M. Pfeifer, J. Pitney, Physical Review Letters, 87 (2001) 195505.
[32] M. Wortis, Chemistry and Physics of Solid Surfaces VII, Springer Berlin Heidelberg Germany, 1988.
[33] C. Giacovazzo, Fundamentals of Crystallography, Third ed., Oxford University Press Inc, United States, 2011.
[34] H. Okamoto, T. Massalski, Bulletin of Alloy Phase Diagrams, 6 (1985) 46-56.
[35] D.J.a.H. Bacon, D., Introduction to Dislocations, Fourth ed., Butterworth-Heinemann, Oxford, UK, 2001.
[36] W. Callister, Materials Science and Engineering: An Introduction, Seventh ed., John Wiley & Sons, Inc., United States, 2007.
[37] P. Heitjans, J. Kärger, Diffusion in Condensed Matter: Methods, Materials, Models, Springer2005.
[38] V. Zielasek, B. Jürgens, C. Schulz, J. Biener, M.M. Biener, A.V. Hamza, M. Bäumer, Angewandte Chemie International Edition, 45 (2006) 8241-8244.
[39] P. Ferreira, Y. Shao-Horn, D. Morgan, R. Makharia, S. Kocha, H. Gasteiger, Journal of The Electrochemical Society, 152 (2005) A2256-A2271.

[40] J. Luo, M.M. Maye, V. Petkov, N.N. Kariuki, L. Wang, P. Njoki, D. Mott, Y. Lin, C.-J. Zhong, Chemistry of materials, 17 (2005) 3086-3091.
[41] Z. Peng, H. Yang, Nano Research, 2 (2009) 406-415.
[42] B.N. Wanjala, J. Luo, B. Fang, D. Mott, C.-J. Zhong, Journal of Materials Chemistry, 21 (2011) 4012-4020.
[43] O. Malis, M. Radu, D. Mott, B. Wanjala, J. Luo, C. Zhong, Nanotechnology, 20 (2009) 245708.